Real-Time Simulation of a Wind Energy System Based on the Doubly-Fed Induction Generator

Lok-Fu Pak, *Student Member, IEEE*, and Venkata Dinavahi, *Senior Member, IEEE*

***Abstract*—This paper presents the real-time digital simulation of a grid-connected wind turbine generator system (WTGS) based on a doubly-fed induction generator (DFIG). A 1.5-MW WTGS is the basis for model development. First a detailed electromagnetic transient model for the WTGS is developed in the MATLAB/SIMULINK environment. This model includes the complete aerodynamic, mechanical and electrical components of the wind turbine, the back-to-back voltage source converter (VSC)-based power electronic interface, as well as the mechanical and electrical controllers of the WTGS. The overall grid-connected WTGS model was then order-reduced and implemented on a PC-cluster-based real-time digital simulator. The maximum execution time of the DFIG model and control was 5.53 μs, while that of the grid-connected WTGS was 15.375 μs. Real-time oscilloscope results are presented to illustrate the WTGS controller performance, the variable wind speed dynamics, and interaction of the WTGS with grid faults. The real-time WTGS model can be readily used for hardware-in-the-loop testing.**

***Index Terms*—Induction generators, power system simulation, real-time systems, wind energy.**

I. Introduction

AMONG many technologies promising green power, the utilization of wind energy via wind turbine generation system (WTGS) is one of the most mature and well developed. Across the world, the total capacity of wind generation is steadily increasing, and larger wind farms are constantly being planned and commissioned [1]–[3]. To understand the impact of this new generation source on the existing power network, and be able to make spontaneous decisions, authentic wind facility models and simulators are required.

There are several offline simulators, such as PSS/E, PSCAD/EMTDC, EMTP, and MATLAB/SIMULINK, that can represent wind generation systems with varying degrees of modeling complexity. The main limitation of such tools is that they lack the ability to be interfaced with physical equipment for testing under real-time conditions. A wind turbine emulator [4]–[6] based on an analog experimental test-bed, on the other hand, provides real-time interaction; however, it is difficult and expensive to setup. Moreover an experimental setup typically includes non-scalable components based on a customized platform requiring constant maintenance, and it is not easily extensible to accommodate large-scale wind farm simulations. A fully digital real-time simulator can overcome obstacles posed by offline and analog simulators. Although research in this area is currently ongoing [7], [8], accurate real-time models for the doubly-fed induction generator (DFIG)-based wind turbines are urgently needed.

To sustain system stability and power quality, sophisticated control and protective devices must be installed to direct the wind facilities through hazardous fault conditions. As the response time of these devices are continuously narrowing, a high resolution wind energy system model suitable for electromagnetic studies is needed for their development, testing, and coordination in real-time. Besides simulating a complex model at high speed, modern real-time simulators are capable of instantaneous communication with external hardware through high resolution input-output (I/O) interfaces. Thus relays, circuit breakers, and controllers can be connected to a real-time simulator in a hardware-in-the-loop (HIL) configuration. The precisely modeled wind facility and transmission system model can then interact with the externally connected equipment in real-time. An engineer can impose any type of faults on the real-time model to evaluate equipment performance. An HIL setup can also help avoid the time consuming and expensive field testing and site trial data recording [9].

Due to its competitive cost and performance, the variable-speed DFIG-based WTGS (Fig. 1) has become the most popular design in the industry [10]. Therefore this paper is focused on modeling the DFIG-based WTGS for real-time electromagnetic simulation studies, and the General Electric (GE) 1.5-MW WTGS [11] is the basis for model development. A detailed electromagnetic transient WTGS model is developed on the widely used graphical simulation platform MATLAB/SIMULINK utilizing its SimPowerSystems (SPS) toolbox. This paper provides a step-by-step illustration of the model development process which makes the model highly customizable. A time-stamped switching function model of the back-to-back PWM VSC precisely accounts for the discrete switching events coming from the controller. After offline verification using PSCAD/EMTDC, and proper model reduction, the grid-connected WTGS model is implemented on the PC-cluster-based real-time simulator [12]. The purpose of developing a fast yet accurate grid-connected WTGS model is to pave the way for the real-time simulation of large-scale wind farms, since offline simulation of such farms can be extremely time consuming.

In the rest of the paper, Sections II and III describe the WTGS model development and system control objectives.

Manuscript received February 04, 2008; revised January 04, 2009. First published May 08, 2009; current version published July 22, 2009. This work was supported by the Natural Science and Engineering Research Council of Canada (NSERC). Paper no. TPWRS-00075-2008.

The authors are with the Department of Electrical and Computer Engineering, University of Alberta, Edmonton, AB T6G 2V4, Canada (e-mail: lokpak@ece.ualberta.ca; dinavahi@ece.ualberta.ca).

Color versions of one or more of the figures in this paper are available online at http://ieeexplore.ieee.org.

Digital Object Identifier 10.1109/TPWRS.2009.2021200

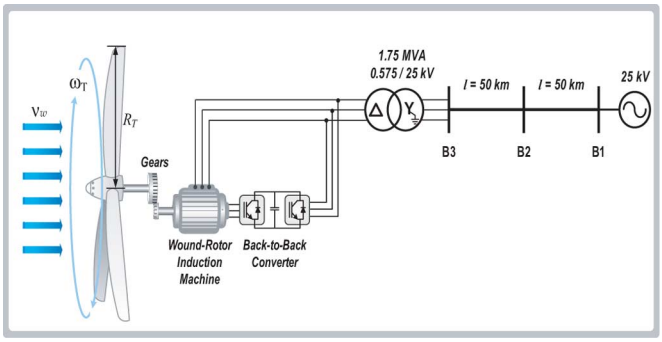

Fig. 1. Doubly-fed induction generator-based WTGS schematic.

Validation of the developed WTGS model and control under real-time conditions is presented in Section IV. In Section V the validated model is applied for the real-time studies of a grid-connected WTGS interacting with varying wind speed and grid faults. Conclusions are given in Section VI.

II. WTGS Model Development and Reduction for Real-Time Simulation

By following the conventional practice [13]–[20] and the manufacturer's documentation [11], a detailed WTGS model based on the GE 1.5-MW concept was developed. The entire system was divided into three submodels: aerodynamic, mechanical, and electrical. Even with a specific manufacturing system as its underlining design, the developed WTGS model does not lose its generality; it can be readily employed for the modeling of the DFIG-based WTGSs from other manufacturers as well.

In this section, emphasis is placed on how to properly apply the necessary reductions to conventional models to achieve real-time simulation in the MATLAB/SIMULINK environment. The amount of detail conserved through the model reduction will be sufficient for characterizing the most critical dynamics of a DFIG-based WTGS.

A. Aerodynamic Model

The aerodynamic model calculates the amount of kinetic energy captured from the wind blowing across the turbine blades. This calculation can get very involved via elemental analysis on the surface of each turbine blade. To avoid such cumbersome analysis, the relatively simple (1) has been generally accepted for estimating the captured kinetic energy in the form of mechanical power (P_{mech}) [11], [15] given as

$$P_{mech} = C_p(\lambda, \theta_{pitch}) \frac{\rho}{2} R_T^2 \pi \nu_w^3 \tag{1}$$

$$\lambda = R_T \left(\frac{\omega_T}{\nu_w} \right). \tag{2}$$

The computation of P_{mech} depends on the power coefficient (C_p), air-density ($\rho \mathrm{kg/m^3}$), turbine radius (R_T m), and wind velocity (ν_w m/s). C_p is a function of the turbine blade tip-speed ratio (λ) and the blade pitch angle (θ_{pitch}). This function describes the percentage of power being extracted from the wind,

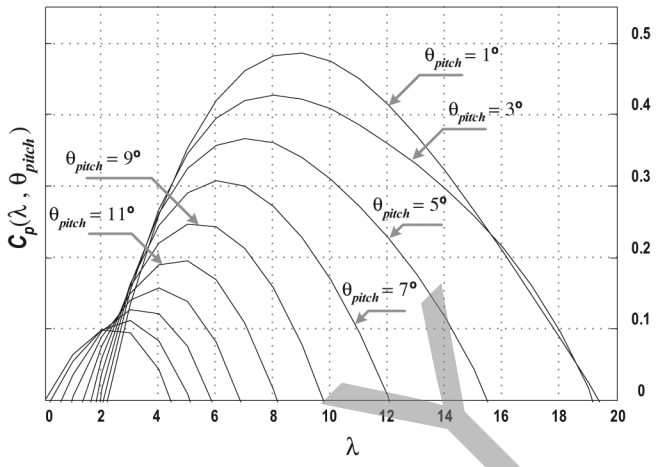

Fig. 2. Reproduction of the GE 1.5-MW WTGS $C_p(\lambda, \theta_{pitch})$ relation using curve fitting (3) in MATLAB.

TABLE I
WTGS Parameters and C_p Coefficients

Aerodynamic model		Rotor mech. model (pu on 1.67MVA base)	
Parameter	Value	Parameter	Value
$\frac{\rho}{2} R_T^2 \pi$	0.00159	H_{1-mass}	4.64
R_T	56.6 ft.	H_{2-mass}	4.32
		H_g	0.62
		K_{tg}	80.27
		D_{tg}	1.5

C_p Coefficients: i, j $\alpha_{i,j}$		
4, 4, $4.9686e^{-10}$	3, 0, $-8.6018e^{-4}$	1, 1, $6.0405e^{-2}$
4, 3, $-7.1535e^{-8}$	2, 4, $2.7937e^{-6}$	1, 0, $-6.7606e^{-2}$
4, 2, $1.6167e^{-6}$	2, 3, $-1.4855e^{-4}$	0, 4, $1.1524e^{-5}$
4, 1, $-9.4839e^{-6}$	2, 2, $2.1495e^{-3}$	0, 3, $-1.3365e^{-4}$
4, 0, $1.4787e^{-5}$	2, 1, $-1.0996e^{-2}$	0, 2, $-1.2406e^{-2}$
3, 4, $-8.9194e^{-8}$	2, 0, $1.5727e^{-2}$	0, 1, $2.1808e^{-1}$
3, 3, $5.9924e^{-6}$	1, 4, $-2.3895e^{-5}$	0, 0, $-4.1909e^{-1}$
3, 2, $-1.0479e^{-4}$	1, 3, $1.0683e^{-3}$	
3, 1, $5.7051e^{-4}$	1, 2, $-1.3934e^{-2}$	

and it is unique for each turbine. λ is calculated with (2), which requires the instantaneous turbine rotational speed (ω_T) and ν_w. θ_{pitch} is given from the mechanical controller depending on the electrical power generation.

The function $C_p(\lambda, \theta_{pitch})$ is usually expressed with a set of parabolic curves. As shown in Fig. 2, the characterizing curves for the GE 1.5-MW system were extrapolated using the curve-fitting formula in the following and the $\alpha_{i,j}$ given in [11]:

$$C_p(\lambda, \theta_{pitch}) = \sum_{i=0}^{4} \sum_{j=0}^{4} \alpha_{i,j} \theta^i \lambda^j. \tag{3}$$

With the parameters provided in Table I, aerodynamic model (1)–(3) were coded in C and inserted as a S-function in SIMULINK. With the input of ν_w, ω_T, and θ_{pitch}, the S-function can accurately calculate P_{mech}.

B. Mechanical Model

The mechanical model replicates the storage and transfer of mechanical energy within the WTGS. As seen from Fig. 1,

the mechanical energy stored in the rotating turbine is transmitted to the generator rotor through two shafts and a set of speed-boosting gears. The entire drive train can be readily represented by the three-mass mechanical model with the springs and dampers representing the torsional losses on the two shafts. However, the direct implementation of this high order model will create excessive demand on computational resources during the simulation of WTGS. In an effort to balance between simulation accuracy and speed, many researchers [11], [20]–[22] have adopted the simplified two-mass model. Solution of the two-mass model can be found with the following equations:

$$\begin{aligned} -T_{elec} &= 2H_g \frac{d\omega_r}{dt} + T_{rs} \\ T_{mech} &= 2H_T \frac{d\omega_T}{dt} - T_{rs} \\ T_{rs} &= (\theta_r - \theta_T)K_{tg} + (\omega_r - \omega_T)D_{tg} \end{aligned} \tag{4}$$

where θ_T and θ_r were the angular position of the turbine and the generator, respectively, found from the integration of ω_T and ω_r (generator rotor rotational speed). Mechanical and electrical torques are represented with T_{mech} and T_{elec}, respectively. K_{tg} and D_{tg} denote the spring constant and damping ratio, respectively; and T_{rs} represents the torque exerted on the high speed shaft.

In SIMULINK, the two-mass model was implemented using the built-in math blocks. The model parameters are given in Table I. With the T_{mech} and T_{elec} provided from the aerodynamic and the machine model, respectively, the two-mass mechanical model will generate the present state T_{rs} to the machine as an input. Nevertheless, it was shown in [23] that the mechanical and electrical isolation established by the DFIG configuration would promise further reduction of the mechanical representation to a single lumped-mass model. The reason was that the fluctuations related to the shaft stiffness could be buffered by the operations of the electrical components when observed from the grid. To solve for this single-mass model, a first-order derivative equation is needed as follows:

$$T_{elec} - T_{mech} = 2H_{lump} \frac{d\omega_{lump}}{dt} \tag{5}$$

where H_{lump} and ω_{lump} indicate the inertia and rotational speed of the lumped mass, respectively. Since the lumped-mass model is already built into the SPS asynchronous machine model [24], the implementation of (5) can be achieved by entering the proper H_{lump} value through the user interface in SIMULINK. Although the single-mass and two-mass models were tested for the real-time simulation, the complexity of the mechanical system can be further increased if desired for higher fidelity of results.

C. Electrical Model

The electrical model can be divided into two main parts: the wound rotor induction machine (WRIM) and the back-to-back converter (BBC) as shown in Fig. 1. Due to their complexity, a large amount of computation time was consumed in solving these electrical models. To satisfy the time constraint for real-time simulation, several model reductions were implemented.

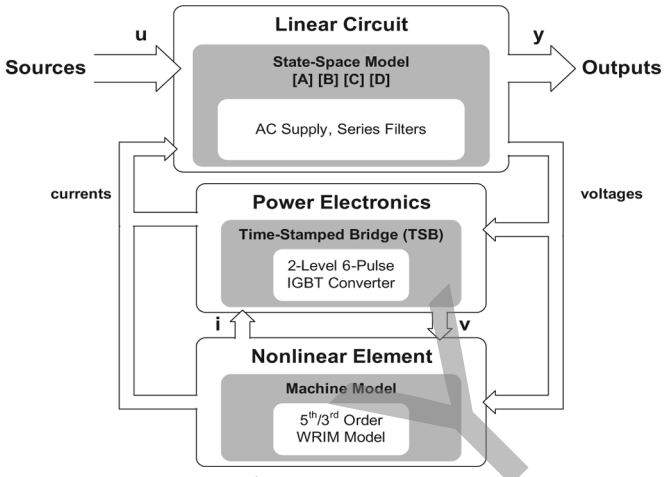

Fig. 3. Electrical system model solution methodology under MATLAB/SIMULINK.

1) Wound-Rotor Induction Machine Model: In SIMULINK, the three-phase WRIM was represented with the Park's model in the arbitrary qd frame. Because of its nonlinear characteristic, the built-in asynchronous machine model [25] from SPS was solved separately as a current feedback module as shown in Fig. 3. With the input voltage (v) from the linear state-space (SS) model, the WRIM model would calculate the qd frame stator and rotor currents using the following equations:

$$\begin{aligned} i_{qs} &= \frac{(\psi_{qs} - \psi_{mq})}{L_{ls}} \quad i_{ds} = \frac{(\psi_{ds} - \psi_{md})}{L_{ls}} \\ i'_{qr} &= \frac{(\psi'_{qr} - \psi_{mq})}{L'_{lr}} \quad i'_{dr} = \frac{(\psi'_{dr} - \psi_{md})}{L'_{lr}} \end{aligned} \tag{6}$$

where

$$\begin{aligned} \psi_{qs} &= \int [v_{qs} - \omega\psi_{ds} - i_{qs}R_s]\omega_b dt \\ \psi_{ds} &= \int [v_{ds} + \omega\psi_{qs} - i_{ds}R_s]\omega_b dt \\ \psi'_{qr} &= \int [v'_{qr} - (\omega - \omega_r)\psi'_{dr} - i'_{qr}R'_r]\omega_b dt \\ \psi'_{dr} &= \int [v'_{dr} + (\omega - \omega_r)\psi'_{qr} - i'_{dr}R'_r]\omega_b dt \end{aligned} \tag{7}$$

$$\begin{aligned} \psi_{md} &= L_{ad}\left(\frac{\psi_{ds}}{L_{ls}} + \frac{\psi'_{dr}}{L'_{lr}}\right) \\ \psi_{mq} &= L_{aq}\left(\frac{\psi_{qs}}{L_{ls}} + \frac{\psi'_{qr}}{L'_{lr}}\right) \\ L_{aq} &= L_{ad} = \frac{1}{\frac{1}{L_m} + \frac{1}{L_{ls}} + \frac{1}{L'_{lr}}}. \end{aligned} \tag{8}$$

The primed parameters symbolize the rotor electrical properties referred to the stator side. R_s and R_r represent the stator and rotor winding resistances, respectively. The leakage inductance of the stator and rotor are expressed by L_{ls} and L_{lr}, respectively. L_m is the magnetizing inductance bonding the stator and rotor

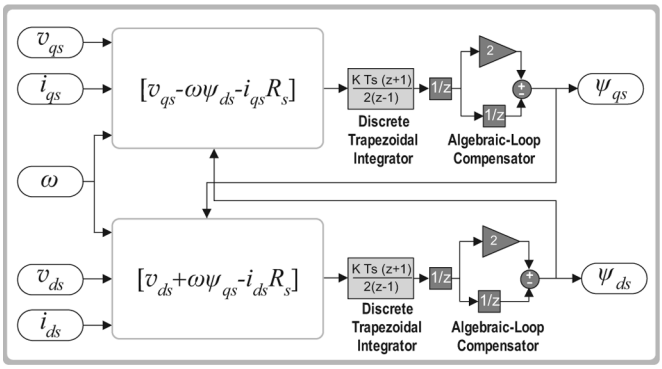

Fig. 4. WRIM model implementation with the trapezoidal integrator and algebraic-loop compensating mechanism.

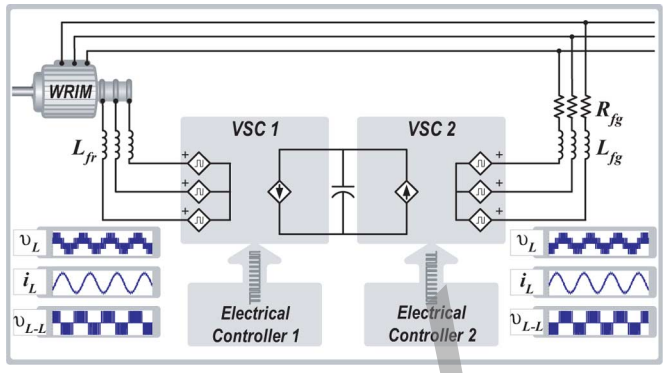

Fig. 5. Time-stamped switching function model for BBC representation.

winding. Magnetic flux in the different windings and axes are indicated with the corresponding ψ terms.

By default, the four integration equations for calculating the magnetic fluxes (ψ) are solved with discrete forward Euler method. In order to improve the accuracy of the machine model while increasing the simulation time-step, the integrations were switched to the more robust discrete trapezoidal method. However, this alteration incurred algebraic-loops in SIMULINK.

When the integration blocks are tracing for the present state values, computations of the elementary blocks involved in the algebraic-loop would be halted temporarily. To break out the algebraic-loop, the common solution would be to insert a delay right after the integration block as shown in Fig. 4. However, this delay will not only break the loop but also affect the stability of the machine model.

To compensate for the addition of a delay, a prediction mechanism was employed. In discrete-time domain, the single step delay is $1/z$, which will create an uncompensated *pole* at the origin of the z-plane. With a prediction function taking the form of

$$G_p(z) = 2 - \frac{1}{z} = \frac{2z-1}{z} \tag{9}$$

in series, the single *pole* will become a compensated double-*pole* constrained by the *zero* created at (0.5, 0). Thus, the overall transfer function for the algebraic-loop compensator is given as

$$G_c(z) = \frac{2z-1}{z^2}. \tag{10}$$

From another point of view, the prediction block improves the estimation of the current state value by calculating the average of the previous state value and the state value obtained at $(t - 2\triangle t)$.

2) Back-to-Back Converter Model: Electrical control exerted upon the WRIM is realized through the switching of the 12 IGBTs contained in the BBC. Essentially, the BBC is constructed from two six-pulse converters connected back-to-back at their dc terminals with the shared buffering capacitor as shown in Fig. 1. In order to efficiently and accurately represent the collective behavior of a six-pulse converter, a time-stamped (TS) switching function model was utilized [12].

In the TS converter model, individual switches are not included. Instead, the model imitates the converter's interactions at ac and dc terminals using controlled voltage and current sources, respectively, as shown in Fig. 5. Since the individual switches are not modeled, representation of the rectifying effect during the shut-off of all the converter switches is not possible. The ac-side voltages are built from the dc voltage and gating pulses while keeping the instantaneous power equal on both sides. This technique is fast as it avoids reformulating SS equations when the converter switch status is changed.

In order to accurately account the switching events occurring between the discrete time-steps [26], the TS model is designed to record the discrete switching events with a 10-ns resolution. From the state and timing information, the TS models can precisely apply the compensation for the omitted switching events. Since the BBC operation involves discrete switchings of the power electronics, current shaping filters are connected at both terminals to limit current distortions.

III. Control Systems

The active power generation set-point (P_{ord}) is extracted from a distinctive power versus ω_r control curve shown in Fig. 6 [14], [16], [18], [19]. For the GE 1.5-MW WTGS, the optimal speed range limited by the converter ratings is defined to be ± 0.3 p.u. of synchronous speed (ω_{sync}) [11]. To overcome system losses, the minimum P_{ord} is fixed to 0.1 p.u. For low-medium ν_w, the control system will maintain the relationship of active power and rotor speed on the curve between points $\mathbf{X}$ and $\mathbf{Y}$ [11]; θ_{pitch} will be kept at zero for maximum power tracking. When ω_T reaches the optimal speed, the control system enters speed-limiting mode until the generated active power reaches the rated limit. Beyond point $\mathbf{Z}$, blade pitch regulation dominates the control and limits the extracted P_{mech}. For very high ν_w, the pitch control will operate before the turbine shut-down speed is reached.

A. Mechanical Control Objectives

The main function of the mechanical control is to regulate the θ_{pitch}, and to generate P_{ord} for the electrical controller. The practical implication of θ_{pitch} control is to regulate P_{mech} under the variable wind condition. When the available wind power is higher than the equipment rating, the turbine blades are pitched to reduce power extraction; as the wind power falls below the

equipment's generation limit, the pitch angle will be kept at minimum to maximize power capturing. The dynamics of the pitch control are moderately fast, and can have significant impact on dynamic simulation results [21]. P_{ord} sent to the electrical controller commands the generator to deliver a certain amount of active power to the grid. The active power actually delivered (P_{elec}) is returned to the mechanical controller for calculating the rotor speed set-point (ω_{ref}). To return ω_r to tracking the optimal generation curve in Fig. 6, the speed error found from $(\omega_r - \omega_{ref})$ is used to drive a PI controller for the renewed P_{ord}. Because of the rapidly reacting power electronics, the dynamics of the power and speed control are very fast.

B. Electrical Control Objectives

Electrical control is accomplished by two independent controllers regulating the two VSCs of the BBC as shown in Fig. 5. Decoupled vector control is the underlying theory that brings the BBC into action.

The electrical controller parameter design procedures given in [14] were successfully applied. For the rotor-side converter (VSC1) maneuvering, the stator-flux oriented indirect voltage control method has been adopted. In the synchronously rotating stator-flux (xy) frame, the stator side active (P_s) and reactive (Q_s) power could be analytically expressed in terms of the orthogonal rotor-side currents i_{ry} and i_{rx}, respectively [20], [27], as follows:

$$P_s = \frac{3}{2}|\vec{V}_s| i_{sy} = -\frac{3}{2}|\vec{V}_s| \frac{L_m}{L_s} i_{ry} \tag{11}$$

$$Q_s = \frac{3}{2}|\vec{V}_s| i_{sx} \approx \frac{3}{2}|\vec{V}_s| \frac{L_m}{L_s} \left(\frac{|\vec{V}_s|}{2\pi f_s L_m} - i_{rx} \right). \tag{12}$$

The grid-side converter control (VSC2) is very similar to that designed for a STATCOM [28]. In the synchronous reference frame aligned with the supply voltage vector, the dc-link voltage and the reactive power flowing to the grid are effectively controlled through the direct- and quadrature-axis currents, respectively.

IV. Verification of the DFIG Configuration and Control

For real-time studies, validation of the model and the reduction techniques developed using SIMULINK was undertaken in two stages. In the first stage, PSCAD/EMTDC were used for offline verification through simulation result comparisons. Under PSCAD/EMTDC, the DFIG configuration and its electrical controller were constructed using the unaltered built-in models. After the reduced-order SIMULINK model and the performance of the controller were validated offline, real-time validation was conducted. Focus of the validation was placed on the accuracy and execution time constraint, which is directly related to the complexity of a given model.

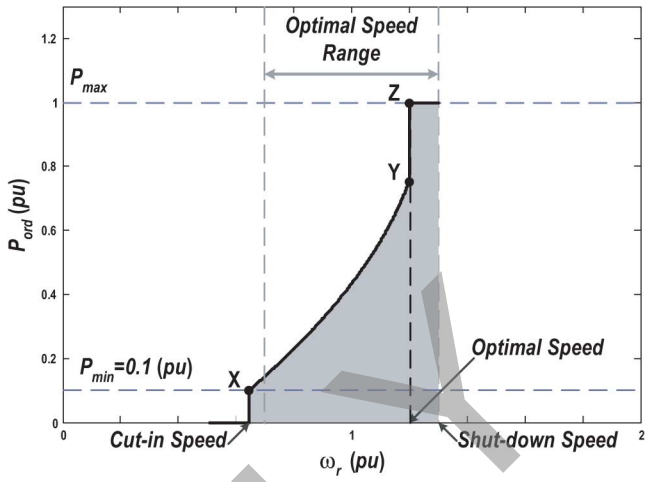

Fig. 6. Power versus generator rotor rotational speed control curve for GE 1.5-MW WTGS.

TABLE II
SS Matrix Dimensions for the DFIG Configuration Built in MATLAB/SIMULINK

Matrix	Original Model Dimensions	Reduced Model Dimensions
A	3 x 3	2 x 2
B	3 x 19	2 x 13
C	29 x 3	19 x 2
D	29 x 19	19 x 13

A. Offline Model Validation and Complexity Assessment in SIMULINK

Close attention has been given to maintain exactness in data entry in both simulation environments (PSCAD/EMTDC and MATLAB/SIMULINK). Thus, any differences in the results would be solely caused due to the inherent modeling and solution techniques involved. To provide adequate resolution for the power electronic model and its control, the simulation time-step was fixed to 50 μs. The offline results in both environments were found to be very similar.

For understanding how the reduction techniques improve the model for real-time simulation, model complexity assessment is the most direct indicator. The objectives of the model reduction are the following: 1) to reduce the size of matrices associated with the linear electrical network, 2) to minimize the total number of states for the complete DFIG configuration, and 3) to break out any algebraic loops in the simulation. The dimensions of the original and reduced-order model state-space matrices are shown in Table II. Various combinations of the WRIM integration method, the BBC model, and the mechanical model were implemented to select the most suitable configuration which can provide a balanced trade-off between accuracy and efficiency. The most appropriate configuration for real-time simulation was found to include the compensated loop-free Trapezoidal integration method for the fifth-order WRIM with a two-mass mechanical model, and the Time-Stamped Bridge model for the BBC.

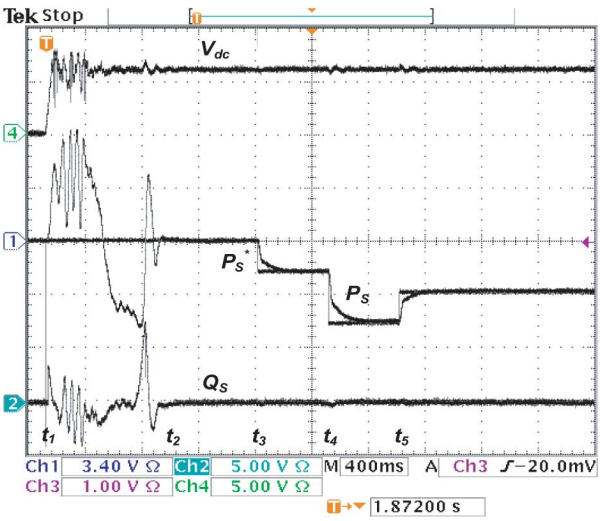

Fig. 7. Oscilloscope trace of the dc-link voltage V_{dc}, stator active power P_s, and stator reactive power Q_s, when P_s is controlled. X-axis: 0.4 s/div., Y-axis: Ch1 (P_s) 0.5 MW/div., Ch2 (Q_s) 0.45 MVar/div., Ch3 (P_s^*) 0.5 MW/div., Ch4 (V_{dc}) 1.0 kV/div.

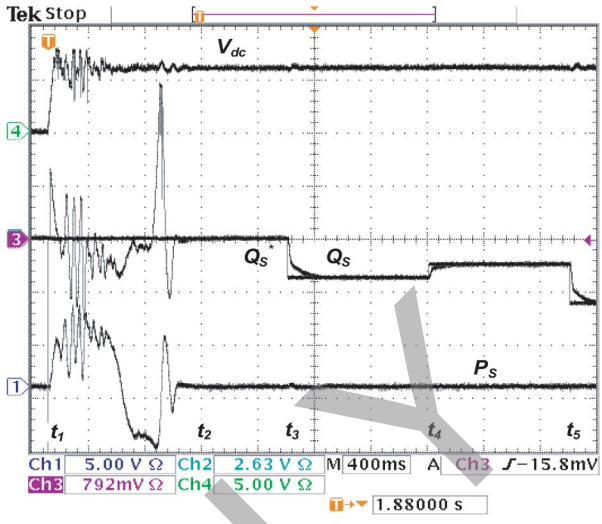

Fig. 8. Oscilloscope trace of the dc-link voltage V_{dc}, stator active power P_s, and stator reactive power Q_s, when Q_s is controlled. X-axis: 0.4 s/div., Y-axis: Ch1 (P_s) 0.5 MW/div., Ch2 (Q_s^*) 0.45 MVar/div., Ch3 (Q_s) 0.45 MVar/div., Ch4 (V_{dc}) 1.0 kV/div.

B. Real-Time Model Validation of the WTGS

The reduced-order configuration was compiled into C code and executed on a 3-GHz Dual-Xeon node of the PC-cluster real-time simulator [12]. One CPU of the computing node was dedicated for the DFIG model implementation, while the other CPU ran the real-time Linux operating system to manage the shared memory data transfer and to interact with peripheral hardware. On a 50 μs time-step, the execution time of the DFIG model was found to be 5.53 μs. By instantaneously sending the simulation results through the high resolution (10 ns) digital output module, the waveforms were recorded using a real-time oscilloscope.

During the 4-s simulation, shown in Figs. 7 and 8, the stator-side active power (P_s), reactive power (Q_s), and dc-link voltage (V_{dc}) were controlled to demonstrate the isolations achieved by the vector control.

After the uncontrolled generator starting transient at time t_1, P_s, and Q_s were steadily maintained at zero until their first step-command occurred. At $t_2 = 1.5$ s, the DFIG was ordered to generate 0.3 MW of active power from the stator. At $t_3 = 0.2$ s later, Q_s was adjusted to -0.3 MVAR. Shortly after Q_s reached its steady state, P_s was furthered to -0.8 MW at $t_4 = 2.0$ s. The final adjustment of P_s occurred at $t_5 = 2.5$ s to -0.5 MW. For Q_s, the last two step commands came at $t_4 = 2.7$ s and $t_5 = 3.7$ s in Fig. 8 with the final values of -0.2 MVAR and -0.5 MVAR, respectively.

In Figs. 7 and 8, a small perturbation can be seen in the P_s waveform whenever a step-change of operating point was made on Q_s and vice versa. This phenomena can be explained by the voltage coupling between the dq parameters. However, vector control has quickly resumed the independence of the control parameters.

V. Real-Time Simulation of a Grid-Connected WTGS

The online performance of a stand-alone WTGS can be easily extended to understand the operation of a wind farm. In this section, the interaction of a DFIG-based WTGS to variable wind source and grid faults are investigated using the power system schematic shown in Fig. 1. Constructed from the detailed DFIG configuration presented in Sections II and III, the WTGS is connected to the 25-kV infinite bus B1 through the distribution transformer and two sections of identical three-phase transmission lines represented with distributed parameter models.

A. Variable Wind Speed Dynamics

The coordination between the mechanical and electrical controllers was verified by applying variable wind speed to the grid-connected WTGS. The variable wind source (ν_w) was made up of four components [19], [23]: average speed, gust, ramp, and turbulence. For the 40-s real-time simulation shown in Fig. 9, the initial turbine speed was set to 0.7 p.u., and the initial power generation from the WRIM was set to zero. To achieve reasonable resolution, the simulation time-step was fixed to 50 μs. The average wind speed for the case study was set to 11.3 m/s. Starting at $t = 0$ s, the parabolic gust was given the amplitude of 3.0 m/s and period of 33.3 s. With the amplitude of 10 m/s and the slope of 0.5 m/s^2, the ramping component was started at $t = 20$ s. Finally, the turbulence was generated as a bandlimited white-noise with variance of 1.2 m/s.

In Fig. 9 the smooth ω_T indicated that the turbine was working as a low-pass filter screening out the effects of the high-frequency turbulence in ν_w. It is easy to notice the 5-s lag between the variations in ν_w and ω_T. This delay was designed into the mechanical controller to prevent the massively spinning turbine from wearing the mechanical components during the abrupt response to the ever-changing wind. The delay was implemented in the model by a simple discrete delay function followed by a rate and saturation limiter.

Before reaching the speed limit of 1.2 p.u., ω_T was directly regulated by altering the active power generation (P_{elec}). Maintaining the proper coordination between ω_T and P_{elec} is critical for the WTGS control. If too much power were extracted, the

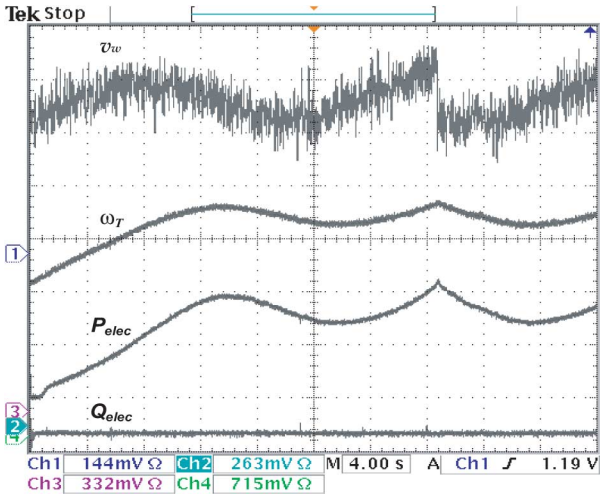

Fig. 9. Oscilloscope trace of final wind velocity v_w, turbine speed ω_T, and electrical powers P_{elec} and Q_{elec} for the grid-connected WTGS. X-axis: 4 s/div., Y-axis: Ch1 (v_w) 4.7 m/s/div., Ch3 (ω_T) 0.3 p.u./div., Ch2 (P_{elec}) 0.3 p.u./div., Ch4 (Q_{elec}) 0.3 p.u./div.

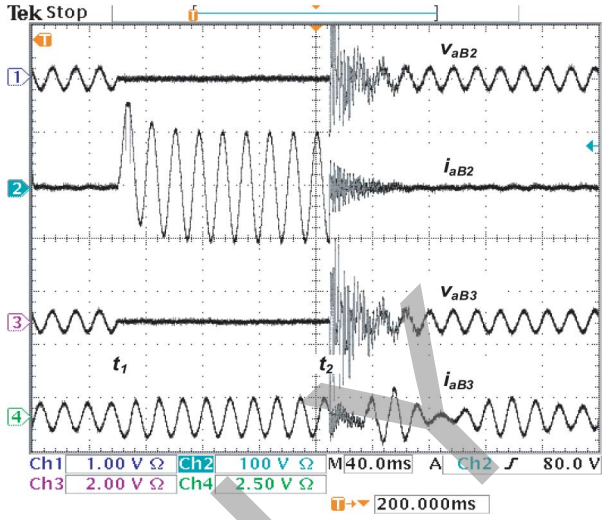

Fig. 10. Oscilloscope trace of voltages and currents due to a 0.15-s duration (t_1 to t_2) single-phase-to-ground fault at Bus B2. X-axis: 0.04 s/div., Y-axis: Ch1 (v_{aB2}) 100 kV/div., Ch2 (i_{aB2}) 1.0 kA/div., Ch3 (v_{aB3}) 50 kV/div., Ch4 (i_{aB3}) 0.07 kA/div.

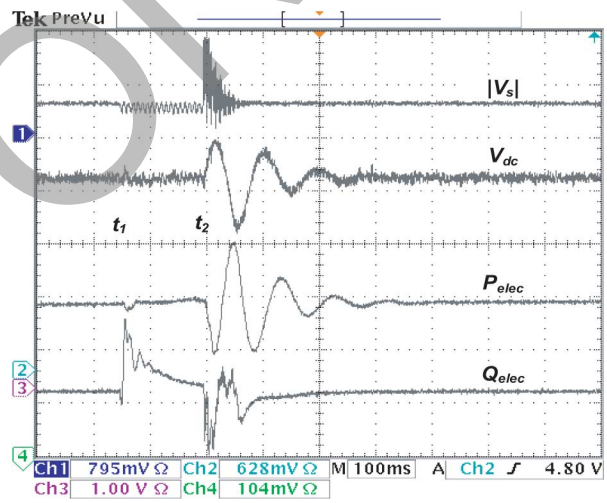

Fig. 11. Oscilloscope trace of WTGS variables due to a 0.15-s duration (t_1 to t_2 single-phase-to-ground fault at Bus B2. X-axis: 0.1 s/div., Y-axis: Ch1 ($|V_s|$) 1.0 p.u./div., Ch2 (P_{elec}) 0.42 p.u./div., Ch3 (Q_{elec}) 0.05 p.u./div., Ch4 (V_{dc}) 0.25 kV/div.

turbine speed would be pushed out of the optimal generation region. On the other hand, insufficient harvesting of the available power would allow the turbine to accelerate to the hazardous speed range. When ω_T reached its limit at $t = 30$ s, active power generation was significantly increased to diffuse the load on the turbine and the mechanical components.

As soon as the generator reached its capacity at $t = 31.8$ s, the pitch control was activated, in order to lessen the amount of power being extracted from the wind. When the ceasing ramp caused a large dip in the available wind power at $t = 32.9$ s, the mechanical controller quickly responded by resetting θ_{pitch} to zero to increase power collection from the turbine, and ordered the electrical controller to reduce P_{elec} to prevent ω_T from collapsing. The real-time simulation results demonstrate that the existing controllers can effectively coordinate the mechanical and electrical parameters to stabilize the WTGS to withstand the disruptive variations, and prepared the entire system for the next rising wave in ν_w. Despite the variations in other system parameters, the vector control has kept the generated reactive power (Q_{elec}) close to zero throughout the entire simulation.

Through the wind speed interaction study, the complete mechanical and electrical controller design was verified. To allow maximum power generation, turbine speed was continuously adjusted in real-time. When the system components reached their limits, proper control sequence was engaged to sustain the stability.

B. Interaction With Grid Faults

Following the WECC low-voltage ride-through standard [1] presented at the California Energy Commission, a case study was setup to examine the reactions of the DFIG-based WTGS to disturbances in the transmission system: a single-line-to-ground fault on the grid for a period of 0.15 s.

Since the focus of this simulation was to study the fault response of the given WTGS, the wind speed was kept constant at 11.3 m/s. To allow fast convergence towards the steady-state, the WTGS was initialized to have the turbine rotation speed (ω_T) = 0.96 p.u., generated active power (P_{elec}) = 0.46 p.u., generated reactive (Q_{elec}) = 0.0 p.u., and BBC dc-link voltage $V_{dc} = 1250$ V. Once the system reached steady-state at $t = t_1$ in Fig. 10, a *9cycle*/0.15 s single-phase-to-ground fault was created in the middle of the transmission system. The transmission system voltages and currents are shown in Fig. 10, while the WTGS variables are shown in Fig. 11. The phase-a voltage at buses B2 and B3 immediately dropped to zero. At the distribution transformer low-voltage side, the loss of phase-a voltage caused disruptive ripples in $|V_s|$ (Fig. 11) which is the magnitude of the WTGS supporting voltage. From the ripples recorded in the waveform of V_{dc}, it was realized that the oscillation in $|V_s|$ has been propagating through the electrical components during the fault.

With phase-a grounding through a small impedance at bus B2, a large unbalanced current was drawn to ground, distorting

the balance along the line, and causing the swelling in phase a and c currents at bus B3.

Under the given fault conditions, the controller was able to maintain the WGTS online. Only a small dip in P_{elec} and Q_{elec} were observed, at the beginning of the fault. This temporary capacity loss was caused by the sudden reduction in average $|V_s|$. As active power generation fell while the mechanical power captured from the wind stayed constant, the turbine accelerated resulting in the increase in reactive power generation. However, the fast acting controller resumed P_{elec} to its pre-fault level within 0.02 s. In order to sustain balance between the mechanical and electrical torque, active power generation was increased to slow down the turbine. Reduction in ω_T was then directly mirrored in the falling of Q_{elec} for the next 0.13 s.

When the fault was normally cleared at $t = t_2$, a large in-rush current from the sudden engagement of phase-a has created high-frequency oscillations in all three phases, shown in the voltage and current waveforms. With relatively low damping in the 50-km line, the oscillations lasted for approximately 0.075 s. At the end of the oscillation, $|V_s|$ was stabilized to its pre-fault value.

From the post-fault response, the grid-side converter controller was found sensitive to the changes in $|V_s|$. When the fault was cleared, the large in-rush current caused a high amplitude jump in $|V_s|$ with the duration less than 0.001 s. However, the controller was sensitive enough to pick up the variation and tried to reset the dc-link voltage. Because the variation in $|V_s|$ was very abrupt, the controller perceived that as a command for step-change in V_{dc}. This was why the signature under-damped response appeared in V_{dc} after the fault, and propagated through the line causing variations in P_{elec}.

By restoring $|V_s|$, a new set-point was reached for ω_T. This abrupt shift in turbine speed has caused minor disturbance in Q_{elec}. Since the speed variation was small (0.02%), Q_{elec} was quickly driven back to its optimal value for unit power generation. With the given shaft stiffness, the multi-mass mechanical system settled to its steady-state in 5 s.

C. Real-Time Performance of the Complete DFIG-Based WTGS

The real-time simulation of the grid-connected WTGS was carried out using two nodes of the PC-cluster real-time digital simulator [12] as shown in Fig. 12. The Master node executed the complete WTGS and the transmission system model, while the Slave node executed the wind speed and fault generator models.

While the wind speed signal and the fault commands were sent from the Slave to the Master subsystems, measurements were simultaneously taken and delivered to the oscilloscope. This high bandwidth communication is centrally managed by the field programmable gate array (FPGA) controlled network interfacing card. The real-time simulation was executed with 50 μs time-step. From the performance log shown in Table III, the maximum computation time was 15.375 μs for the Master subsystem. To finish the execution cycle for the Slave subsystem, only 2.257 μs was needed. Including the 6.628 μs overhead for communication, the maximum execution time was still well

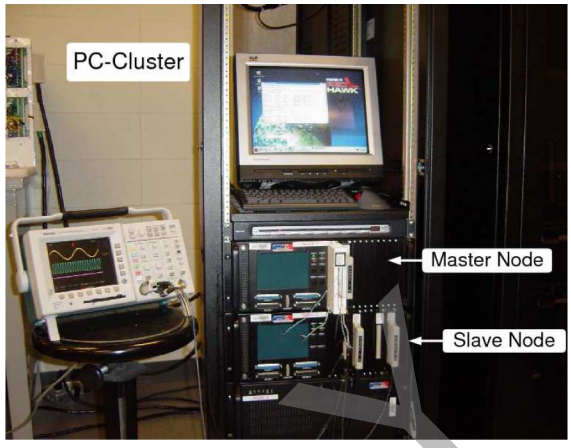

Fig. 12. Real-time digital simulator setup.

TABLE III
PERFORMANCE LOG FOR THE REAL-TIME SIMULATION OF THE GRID-CONNECTED WTGS SHOWN IN FIG. 10

Task	Master (μs)	Slave (μs)
Computation Time	15.375	2.257
Idle Time	24.770	39.819
Data Acquisition	0.995	0.305
Status Update	0.290	0.290
Target Request Time	0.062	0.067
Host Request Time	0.045	0.047
Synchronization	0.075	0.054
Signal To Master	–	6.628
Signal From Master	–	–
Signal To Slave	–	–
Signal From Slave	6.628	–
Others	0.840	0.533
Total Time-step	50	50

below 50 μs, indicating that the simulator was being under utilized. Over the 40-s simulation time frame, the simulator was able to perform the complex model computation while supervising the intensive communication among different hardware components.

VI. CONCLUSIONS

This paper proposes a highly customizable real-time model of a DFIG-based grid-connected WTGS. This accurate and efficient model was developed on a PC-cluster-based real-time simulator. Employing the widely used MATLAB/SIMULINK environment, a detailed electromagnetic transient model is constructed for the WTGS, based on the GE 1.5-MW DFIG, including the WRIM, the BBC, and the various mechanical and electrical controllers. After rigorous offline verification using the PSCAD/EMTDC software, several model reductions were implemented to make the model suitable for real-time simulation. The execution time of the single WTGS model was 5.53 μs on a time-step of 50 μs. Real-time oscilloscope results are shown to prove the accuracy and validity of the developed model. Recordings of the uncontrolled high-frequency starting transient in the waveforms demonstrate the level of resolution that was achieved by the real-time WTGS model.

The stand-alone WTGS model was then linked to a transmission system model to study the impact of grid conditions on the WTGS. From the presented case studies, the complete WTGS

model has demonstrated its capability to generate power under varying wind conditions while riding through unbalanced grid faults. The execution time of the grid-connected WTGS model was 15.375 μs on a time-step of 50 μs. With the developed real-time model, new controller designs or protective devices can be easily implemented and tested in a HIL configuration. It is also possible to include multiple WTGS models to achieve a real-time wind farm simulation.

REFERENCES

[1] R. Zavadil, N. Miller, A. Ellis, and E. Muljadi, "Making connections," *IEEE Power Energy Mag.*, vol. 3, no. 6, pp. 26–37, Nov./Dec. 2005.

[2] P. B. Eriksen, T. Ackermann, H. Abildgaard, P. Smith, W. Winter, and J. R. Garcáa, "System operation with high wind penetration," *IEEE Power Energy Mag.*, vol. 3, no. 6, pp. 65–75, Nov./Dec. 2005.

[3] R. Piwko, D. Osborn, R. Gramlich, G. Jordan, D. Hawkins, and K. Porter, "Wind energy delivery issues," *IEEE Power Energy Mag.*, vol. 3, no. 6, pp. 47–56, Nov./Dec. 2005.

[4] H. M. Kojabadi, L. Chang, and T. Boutot, "Development of a novel wind turbine simulator for wind energy conversion systems using an inverter-controlled induction motor," *IEEE Trans. Energy Convers.*, vol. 19, pp. 547–552, Sep. 2004.

[5] M. G. Jovanović, R. E. Betz, and J. Yu, "The use of doubly fed reluctance machines for large pumps and wind turbines," *IEEE Trans. Ind. Appl.*, vol. 38, pp. 1508–1516, Nov.–Dec. 2002.

[6] T. F. Chan, K. A. Nigim, and L. L. Lai, "Voltage and frequency control of self-excited slip-ring induction generators," *IEEE Trans. Energy Convers.*, vol. 19, pp. 81–86, Mar. 2004.

[7] C. Nichita, D. Luca, B. Dakyo, and E. Ceanga, "Large band simulation of the wind speed for real time wind turbine simulators," *IEEE Trans. Energy Convers.*, vol. 17, pp. 523–529, Dec. 2002.

[8] M. Steurer, H. Li, S. Woodruff, K. Shi, and D. Zhang, "Development of a unified design, test, and research platform for wind energy systems based on hardware-in-the-loop real-time simulation," in *Proc. IEEE Power Electronics Specialists Conf.*, Aachen, Germany, 2004, pp. 3604–3608.

[9] S. J. Haslam, P. A. Crossley, and N. Jenkins, "Design and field testing of a source based protection relay for wind farms," *IEEE Trans. Power Del.*, vol. 14, no. 3, pp. 818–823, Jul. 1999.

[10] P. Pourbeik, R. J. Koessler, D. L. Dickmander, and W. Wong, "Integration of large wind farms into utility grids part II—performance issues," in *Proc. IEEE PES General Meeting*, Jul. 2003, vol. 3, pp. 13–17.

[11] N. W. Miller, W. W. Price, and J. J. Sanchez-Gasca, "Dynamic modeling of GE 1.5 and 3.6 wind turbine-generators," *GE-Power Syst. Energy Consult.*, pp. 1–31, 2003.

[12] L.-F. Pak, M. O. Faruque, X. Nie, and V. Dinavahi, "A versatile cluster-based real-time digital simulator for power engineering research," *IEEE Trans. Power Syst.*, vol. 21, no. 2, pp. 455–465, May 2006.

[13] O. Wasynczuk, D. T. Man, and J. P. Sullivan, "Dynamic behavior of a class of wind turbine generators during random wind fluctuations," *IEEE Trans. Power App. Syst.*, vol. PAS-100, pp. 2837–2845, Jun. 1981.

[14] R. Pena, J. C. Clare, and G. M. Asher, "Doubly fed induction generator using back-to-back PWM converters and its application to variable-speed wind-energy generation," *Proc. Inst. Elect. Eng., Elect. Power Appl.*, vol. 143, no. 3, pp. 231–241, May 1996.

[15] S. Heier, *Grid Intergration of Wind Energy Coversion Systems*. Chichester, U.K.: Wiley, 1998.

[16] S. A. Papathanassiou and M. P. Papadopoulos, "Dynamic behavior of variable speedwind turbines under stochasticwind," *IEEE Trans. Energy Convers.*, vol. 14, pp. 1617–1623, Dec. 1999.

[17] T. Petru and T. Thiringer, "Modeling of wind turbines for power system studies," *IEEE Trans. Power Syst.*, vol. 17, no. 4, pp. 1132–1139, Nov. 2002.

[18] R. Datta and V. T. Ranganathan, "Variable-speed wind power generation using doubly fed wound rotor induction machine—a comparison with alternative schemes," *IEEE Trans. Energy Convers.*, vol. 17, pp. 414–420, Sep. 2002.

[19] J. G. Slootweg, S. W. H. de Haan, H. Polinder, and W. L. Kling, "General model for representing variable speed wind turbines in power system dynamics simulations," *IEEE Trans. Power Syst.*, vol. 18, no. 1, pp. 144–151, Feb. 2003.

[20] A. Tapia, G. Tapia, J. X. Ostolaza, and J. R. Sáenz, "Modeling and control of a wind turbine driven doubly fed induction generator," *IEEE Trans. Energy Convers.*, vol. 18, pp. 194–204, Jun. 2003.

[21] S. K. Salman and A. L. J. Teo, "Windmill modeling consideration and factors influencing the stability of a grid-connected wind power-based embedded generator," *IEEE Trans. Power Syst.*, vol. 18, no. 2, pp. 793–802, May 2003.

[22] C. Carrillo, A. E. Feijóo, J. Cidrás, and J. González, "Power fluctuations in an isolated wind plant," *IEEE Trans. Energy Convers.*, vol. 19, pp. 217–221, Mar. 2004.

[23] J. G. Slootweg, S. W. H. de Haan, H. Polinder, and W. L. Kling, "Aggregated modelling of wind parks with variable speed wind turbines in power system dynamics simulations," in *Proc. 14th Power Systems Computation Conf.*, Sevilla, Spain, Jun. 2002.

[24] G. Sybille, L. A. Dessaint, P. Giroux, R. Gagnon, S. Casorla, P. Brunelle, R. Champagne, H. Le-Huy, L. A. Dessaint, H. Fortin-Blanchette, C. Semaille, and P. Mercier, *SimPowerSystems For Use with Simulink User's Guide Version 4*. Montreal, QC, Canada: Hydro-Québec, TransÉnergie Technologies.

[25] G. Sybille, P. Brunelle, L.-H. Hoang, L. A. Dessaint, and K. Al-Haddad, "Theory and applications of power system blockset, a MATLAB/simulink-based simulation tool for power systems," in *Proc. IEEE PES Winter Meeting, 2000*, Jan. 23–27, 2000, vol. 1, pp. 771–779.

[26] V. R. Dinavahi, M. R. Iravani, and R. Bonert, "Real-time digital simulation of power electronic apparatus interfaced with digital controllers," *IEEE Trans. Power Del.*, vol. 16, no. 4, pp. 775–781, Oct. 2001.

[27] P. Vas, *Vector Control of AC Machines*. New York: Oxford Univ. Press, 1990.

[28] C. Schauder and H. Mehta, "Vector analysis and control of advanced static var compensators," *Proc. Inst. Elect. Eng., Gen., Transm., Distrib.*, vol. 140, no. 4, pp. 299–306, Jul. 1993.

Lok-Fu Pak (S'03) received the B.Sc. degree in electrical engineering and M.Sc. degree in electrical and computer engineering from the University of Alberta, Edmonton, AB, Canada, in 2003 and 2006, respectively.

His research interests include renewable energy, wind turbine generation, electromagnetic transient simulation of FACTS, power electronics, and real-time simulation of power systems. He is currently employed with Suncor Energy, Inc., Calgary, AB, Canada

Venkata Dinavahi (M'00–SM'08) received the Ph.D. degree in electrical and computer engineering from the University of Toronto, Toronto, ON, Canada, in 2000.

Presently, he is an Associate Professor at the University of Alberta, Edmonton, AB, Canada. His research interests include electromagnetic transients, power electronics, and real-time digital simulation and control.